Dipolar coupling effect on magnetization dynamics in artificial kagome spin ices

Xi Shen,[1,*] Haoran Chen,[1,*] Dong Shi,[2] Hong Xia,[1] Jia Xu,[3] Fanlong Zeng,[1] and Yizheng Wu [1,4,†]

[1]*Department of Physics and State Key Laboratory of Surface Physics, Fudan University, Shanghai 200433, China*
[2]*School of Physical Science and Technology, ShanghaiTech University, Shanghai 200031, China*
[3]*Institute of Physics, Shaanxi University of Technology, Hanzhong 723001, China*
[4]*Shanghai Research Center for Quantum Sciences, Shanghai 201315, China*

The study of spin dynamics in artificial spin ice (ASI) has in recent years become a vibrant research field for reconfigurable magnonics. We present experimental and theoretical studies of magnetization dynamics in disconnected kagome ASI lattices using broadband ferromagnetic resonance and micromagnetic simulations. By systematically varying the field strength and orientation, the dynamical coupling effects between different ASI sublattices have been distinguished for the field along the symmetric axes. For the field parallel to one sublattice bar, the mode hybridization with an avoided-crossing gap is identified, and a special dynamical magnon mode emerges. But, for the field perpendicular to one sublattice bar, the magnon modes from the other two sublattice bars merge into a single mode, which is attributed to the static dipolar interactions between the sublattice bars. Our research shows a detailed investigation of magnetization dynamics in kagome ASIs, which is of great significance to further understand collective spin-dynamics behavior in nanomagnet systems.

I. INTRODUCTION

Artificial spin ice (ASI) is a two-dimensional geometrically arranged magnetic frustration structure composed of interacting nanomagnets [1,2], and was initially introduced to simulate atomic-scale magnetic frustration and monopole-like excitations in spin ice materials with the advantage that the magnetization states in ASI could be directly observed using magnetic microscopy techniques [3–5]. These nanomagnets have an elongated shape with a bistable magnetic behavior, and are usually referred to as macrospins. Through magnetic field-driven and thermal relaxation processes, degenerate ground states and magnetization reversal in ASI have been intensively studied [6–8]. The magnetization-reversal process in spin ice structures is usually governed by the ice rule due to the dipolar interaction between neighboring macrospins. Therefore, ASI structures can provide deep insight into the fundamental understanding of magnetic properties induced by complex magnetic frustrations [9–12].

Magnetization dynamics in ASIs have also recently attracted increasing interest [13–31], since the periodic arrangements in ASIs provide an ideal framework for manipulating spin-wave propagation in the field of magnonics [20,21]. Magnetization dynamics properties are associated with the magnetization configuration; thus, reconfigurable magnetic microstates make ASIs a promising system to investigate reprogrammable magnonics [17,22]. Previous investigations on magnetization dynamics in square-type and kagome-type ASIs usually studied the bulklike mode of ferromagnetic resonance (FMR), which are contributed from the resonance mode of the macrospins in each sublattice [13,18,23,24]. The contributions of the different FMR modes from different sublattices were further identified through Brillouin scattering [25,30], micromagnetic simulations [26], or through experimental modifications of shape anisotropy of different sublattices in ASIs [27–29]. Topological defects in the magnetization-switching process were discovered to significantly modify microscopical magnon modes in ASIs [17,19]. Besides the magnon modes located in each nanomagnet, a special mode localized in the vertex region was recently discovered due to the direct exchange coupling between two macrospins [31].

Although magnetization dynamics in ASIs have been proved to associate with the magnetic microstates during the magnetization-reversal process [15,19,30], very little attention has been paid to investigate the effect of dipolar coupling on magnetic dynamics properties in ASIs. Recent studies in a bicomponent square-type ASI demonstrated the existence of the microstate-dependent mode hybridization and anticrossings [32], which is attributed to the significant dynamic dipolar coupling [33]. Thus, the mode hybridization in more ASI systems is also expected. The magnon coupling usually shows its maximum effect when two magnon modes are energy degenerated [34,35]. In ASIs, varying the orientation of the applied magnetic field can modify the degeneracy of magnon modes located in different sublattices; thus, it is expected that the coupling effect due to dipolar interaction can be systematically tuned by varying the degeneracy of magnon modes in different sublattices with the field orientation.

In this work, we studied magnetization dynamics in disconnected kagome ASIs using broadband FMR measurements and micromagnetic simulations. Obvious changes of the FMR spectra are observed due to the magnetization switching,

---

*These authors contributed equally to this work.
†wuyizheng@fudan.edu.cn
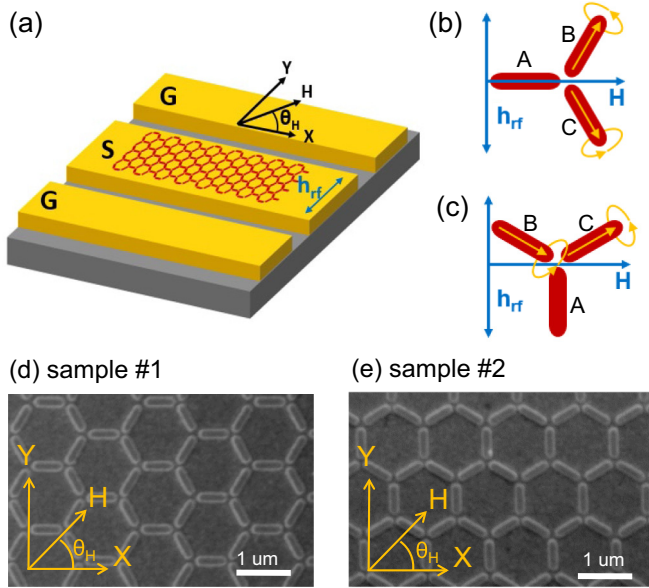
FIG. 1. (a) Schematic of sample for the FMR measurements. (b), (c) Schematic of magnetic dynamics in a vertex of kagome ASI with the applied field **H** (b) parallel to the A bars and (c) perpendicular to the A bars. (d), (e) SEM images of samples No. 1 and No. 2 with different orientation with respect to the signal line along the x axis.

consistent with previous reports [7,10,23–26,36–38]. We investigated the evolution of the magnon modes by gradually changing the strength and the orientation of the applied field, and directly observed the effect of magnon coupling for the field along the symmetric directions of the ASIs. For the field parallel to one sublattice bar, except the avoided-crossing gap due to the mode-hybridization effect, an additional dynamical magnon mode emerges, which is identified as a spin-wave mode through micromagnetic simulation. However, for the field perpendicular to one sublattice bar, we find that the magnon modes from the other two sublattice bars merge into a single mode, which is attributed to the effect of static dipolar interactions between the sublattice bars. Our results confirm the existence of magnon coupling in the ASI lattices, which may further influence the reconfigurable spin-wave propagation in magnonics devices based on ASIs [17,22].

II. EXPERIMENTS AND SIMULATION METHOD

Figure 1(a) shows the sample structure for FMR measurements. The coplanar waveguide (CPW) made of Cr/Au (3 nm/150 nm) was fabricated by magnetron sputtering on the Si/SiO$_2$ substrates; the width of signal line S is 20 μm and the width of the gap between signal line S and ground line G is 8 μm. The kagome ASI was patterned on top of the signal line by electron-beam lithography, followed by electron-beam evaporation and lift-off of permalloy (Py, Ni$_{80}$Fe$_{20}$). The dimensions of the magnetic bars are 560 nm in length and 120 nm in width with a thickness of 15 nm [37,39]. The microwave transmission signal S_{21} was measured by a vector network analyzer, and the magnetic field **H** was provided by a vector magnet, so **H** could rotate in the sample plane with a field

angle θ_H respective to the signal line. The microwave with a 0−dB m power was applied in the measurements.

The kagome lattice consists of three sublattice branches (described as A, B, and C) with an intersection angle of 120° between magnetic bars, so there are two kinds of symmetry axes in the kagome lattice for **H** parallel or perpendicular to one type of bars in the kagome lattice, as described in Figs. 1(b) and 1(c). The other two types of bars (B and C) should have the identical dynamical properties; thus, the magnetic coupling between B and C bars is expected to modify the dynamical properties of the system. In order to ensure the identical excitation on B and C bars by the microwave magnetic field **h**$_{rf}$, we prepared two types of samples. In sample No. 1, the A bars are parallel to the signal line; thus, **h**$_{rf}$ is perpendicular to the A bars. In sample No. 2, the A bars are perpendicular to the signal line with **h**$_{rf}$ parallel to the A bars. The magnetization alignment in B and C bars is different for samples No. 1 and No. 2, so the dynamical coupling in these two samples is also expected to be different. Figures 1(d) and 1(e) show the representative images of the two samples measured by the secondary electron microscope (SEM).

In order to further understand the origin of the dynamics coupling effect, we performed micromagnetic simulations using the graphic processing unit accelerated software MUMAX3 [40,41]. The ASI in the simulation has the same dimension as that in the experimental system, and each nanomagnet has a half-circle end with a length of 560 nm, width of 120 nm, and thickness of 15 nm. We applied the standard magnetic parameters for Py, such as saturated magnetization $M_s = 700$ kA/m, exchange stiffness parameter $A = 10$ pJ/m, gyromagnetic ratio $\gamma = 185$ rad GHz/T, and damping constant $\alpha = 0.05$, and the sample was discretized into elemental cells of $5 \times 5 \times 15$ nm^3. While applying H with a particular angle θ_H, an in-plane field pulse $h(t) = h_0 \sin[\pi f_c(t - t_0)]/\pi f_c(t - t_0)$ perpendicular to **H** with $f_c = 40$ GHz and $h_0 = 0.1$ mT is applied to excite the eigenmodes in the ASI system [42]. The transient dynamics were computed over 15 ns, with the data taken every 5 ps. We calculated the z-component magnetization fluctuations at time t, i.e., $\delta m_z(t) = m_z(t) - m_z(0)$, where $m_z(0)$ corresponds to the magnetization of each magnetic unit at the equilibrium state. Then, the power spectrum $s(f)$ is computed through the Fourier transform of $\delta m_z(t)$, i.e., $s(f) = |\int_0^{t_0} e^{-i2\pi f t} \delta m_z(t) dt|$, where t_0 represents the total duration of the time integration performed in the simulations. The spatial profiles can be obtained by $s(f)$ of each cell at a given frequency f and applied field **H**. The total FMR spectrum $S(f)$ can be calculated by integrating $s(f)$ of all the cells in the ASI structure, i.e., $S(f) = \sum s(f)$.

III. RESULTS AND DISCUSSION

A. Field-dependent resonance spectra of kagome ASIs

We first measured the hysteresis loops of the ASI samples utilizing high-resolution Kerr microscopy [37]. Figure 2(a) shows the typical hysteresis loops from sample No. 1 with different θ_H. For $\theta_H = 0°$ with H along one of the bars, the hysteresis loop shows the single-step switching behavior with the switching field $Hc_1 = 250$ Oe. For $\theta_H = 15°$ and 30°, the magnetization reversal presents a two-step process. The first
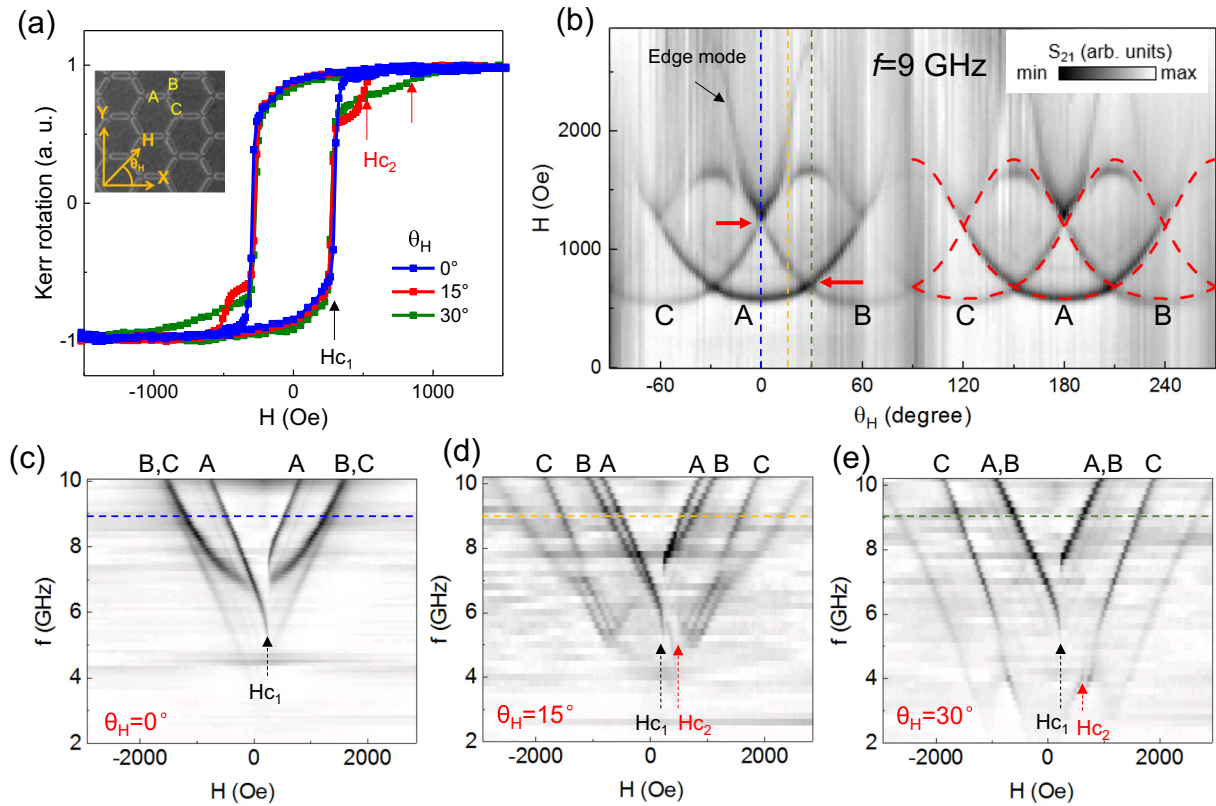
FIG. 2. (a) Normalized hysteresis loops from sample No. 1 with different θ_H. Inset shows the SEM image of the sample with three sublattice bars identified as A, B, and C. (b) H-θ_H absorption spectra of sample No. 1 with a fixed microwave frequency of $f = 9$ GHz. Red dashed lines are the calculated resonant fields H_r of three sublattice bars with an effective uniaxial anisotropy field of 310 Oe. (c)–(e) f-H spectra measured with $\theta_H = 0°$, $15°$, and $30°$. Horizontal dashed lines in (c)–(e) correspond to the signals in the H-θ_H spectra marked as the vertical dashed lines in (b). Corresponding bars of different major FMR modes in (b)–(e) are marked in each figure.

switching field is independent of θ_H with $Hc_1 \sim 250$ Oe, and the second switching field Hc_2 is 550 Oe for $\theta_H = 15°$ and 800 Oe for $\theta_H = 30°$. Our results are consistent with the reported magnetization-reversal behaviors with a sixfold symmetry in the kagome ASI lattice [36,37,39]. As demonstrated by real-space imaging in Ref. [37], the magnetization switches with two-dimensional avalanches for the field applied along one of the sublattice branches, and for $0° < \theta_H < 30°$, the magnetization first switches with discrete one-dimensional Dirac strings at Hc_1, followed by the magnetization switch of the third bar at Hc_2.

Microwave absorption measurements were obtained by measuring the transmission parameter S_{21} while sweeping the field **H** along different orientations with θ_H respective to the signal line. Figure 2(b) shows the H-θ_H absorption spectra of sample No. 1 with a fixed frequency $f = 9$ GHz. The absorption signal was measured with **H** sweeping from 0 to 2800 Oe at different θ_H varying from $-90°$ to $270°$. Since the microwave field $\mathbf{h}_{rf}$ is perpendicular to the signal line, it is expected that the maximum absorption intensity is observed for θ_H near $0°$ and $180°$. For $\theta_H \sim 90°$ and $270°$, the adsorption signal is weak due to the parallel alignment between **H** and $\mathbf{h}_{rf}$. The adsorption spectra in Fig. 2(b) clearly display the multimode resonances with a sixfold angular-dependent symmetry. According to reports in the literature [19,26,43], the main resonance signals in Fig. 2(b) with the resonance field H_r less than 1700 Oe are the uniform FMR modes from

different sublattice bars. The weaker resonance signals with $H_r > 1700$ Oe are from the edge modes of different bars [26,43]. The main FMR mode in each sublattice bar can be calculated through the magnetic uniaxial anisotropy due to the shape anisotropy. In Fig. 2(b), we plot the calculated θ_H-dependent H_r of each sublattice bar with the red dashed lines for θ_H between $90°$ and $270°$, which are in good agreement with the experimental data.

To better characterize each resonance mode, we measured the f-H absorption spectra with fixed θ_H. Figures 2(c)–2(e) show the typical f-H absorption spectra with $\theta_H = 0°$, $15°$, and $30°$ from sample No. 1. During the measurement, H was swept from -3000 to 3000 Oe with f varying from 1 to 10 GHz. The horizontal dashed lines in Figs. 2(c)–2(e) marked at $f = 9$ GHz correspond to the vertical dashed lines in the H-θ_H spectra in Fig. 2(b). The measured f-H spectra with different θ_Hs agree well with those in artificial kagome spin ice vertices made of three identical nanoislands [31], indicating that the major resonant modes are the Kittel-like modes from the individual sublattice bars. The corresponding bars for each bulk resonant mode are also marked on top of Figs. 2(c)–2(e). The edge mode can also be observed for the large field around 2000 Oe in Figs. 2(d) and 2(e). Besides the bulk modes and edge modes, we can also observe some weak resonant modes, which should be the spin-wave modes inside the magnetic bars [25] and are not the focus of our studies. The f-H spectra in Figs. 2(c)–2(e) also demonstrate
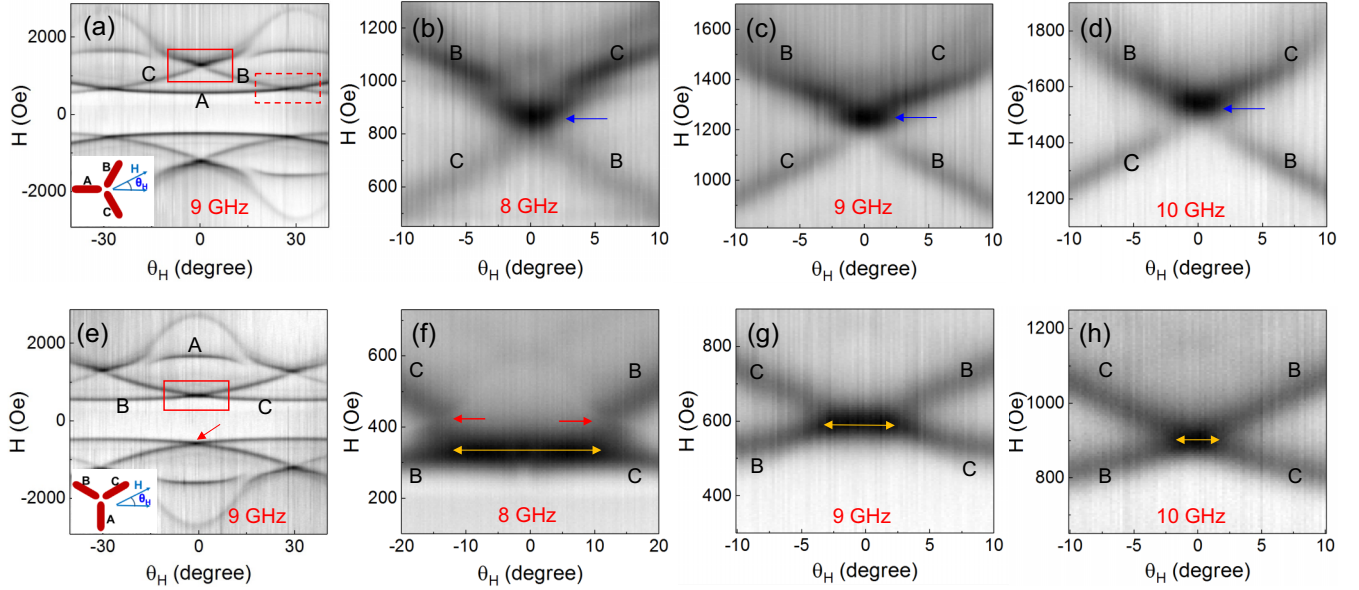
FIG. 3. (a) H-θ_H spectra at $f = 9$ GHz for sample No. 1. Inset shows the schematic of sample geometry. Red solid and dashed squares emphasize the features at $\theta_H = 0°$ and $30°$, respectively. (b)–(d) Enlarged H-θ_H spectra at $f = 8$, 9, and 10 GHz, respectively, around $\theta_H = 0°$ for sample No. 1. Blue arrows in (b)–(d) indicate the magnon mode at $\theta_H \sim 0°$. (e) H-θ_H spectra at $f = 9$ GHz for sample No. 2. (f)–(h) Enlarged H-θ_H spectra at $f = 8$, 9, and 10 GHz, respectively, around $\theta_H = 0°$ for sample No. 2. Horizontal yellow arrows in (f)–(h) indicate the angular range of the single mode decreases with f, and red arrows in (f) emphasize the discontinuity of the magnon mode.

that the measured dynamics modes correspond to different magnetization states [28]. For $\theta_H = 0°$ in Fig. 2(c), there is an abrupt change of dynamical dispersion at ~ 200 Oe, and this corresponds to the coercive field Hc_1 for all the bars due to two-dimensional avalanche switching for $\theta_H = 0°$ [10,37]. For $\theta_H = 15°$ and $30°$, two abrupt changes can be identified, as marked by the arrows in Figs. 2(d) and 2(e). The first field change at Hc_1 is due to the formation of Dirac strings along the A and B bars, and the second change at Hc_2 is due to the magnetization switching of the bars perpendicular to the Dirac strings [37,39]. The determined Hc_1 for $\theta_H = 15°$ and $30°$ are ~ 200 Oe, and the measured values of Hc_2 are ~ 450 Oe for $\theta_H = 15°$ and ~ 650 Oe for $\theta_H = 30°$. It should be noted that the determined Hc_1 and Hc_2 from the dynamics spectra are significantly smaller than the values determined by the hysteresis loops in Fig. 2(a), which can be attributed to microwave-assisted magnetization switching [44].

B. Angular-dependent resonance spectra of kagome ASIs

In Fig. 2(b), the resonant fields of B and C bars have a crossover at $H \sim 1200$ Oe for $\theta_H = 0°$; thus, at this crossover condition, the magnetization dynamics in B and C bars are degenerated, and the magnetic coupling may break the degeneracy, which can be investigated by continuously varying the field angle. We further performed a fine measurement of the H-θ_H spectra with a field step of 5 Oe and an angular step of $0.5°$. Figure 3(a) shows the measured H-θ_H spectra of sample No. 1 at $f = 9$ GHz with the field sweeping from -3000 to $+3000$ Oe, which can better resolve the angular-dependent dynamical behavior in comparison with the data in Fig. 2(b). In order to better identify the coupling effect of the two dynamical modes from the B and C bars emphasized by the red solid rectangle in Fig. 3(a), we further performed the fine

scan of H-θ_H spectra around the crossing point with different microwave frequencies. Figures 3(b)–3(d) show the measured H-θ_H spectra around the crossing point at 8, 9, and 10 GHz, respectively. For larger $|\theta_H|$, there are two separated FMR modes from B and C bars, and the difference between two resonant fields H_r increases with $|\theta_H|$. The dynamical mode with higher H_r has the higher adsorption intensity, but the intensity of the mode with lower H_r is relatively weaker, and becomes very small for $|\theta_H| < 2°$. Moreover, for $\theta_H \approx 0°$, there is another clear resonant mode with the intensity much stronger than the other FMR modes at large $|\theta_H|$, and this emerging resonant mode may indicate the mode-hybridization effect.

As shown in Fig. 1(c), for the field perpendicular to one sublattice bar, the FMR modes from the other two sublattice bars are degenerated. For sample No. 1, as indicated by the sample structure in the inset in Fig. 3(a), the resonant mode from A and B bars should also have a crossover at $\theta_H = 30°$. However, because the microwave field $\mathbf{h}_{rf}$ is always perpendicular to A bars, the FMR modes of A and B bars always show different intensity at $\theta_H \approx 30°$, as indicated by the red dashed rectangle in Fig. 3(a). So, in order to better understand the dynamical coupling effect for the field perpendicular to one of the three sublattice bars, we performed careful studies with the field sweeping from -3000 to 3000 Oe on sample No. 2, in which $\mathbf{h}_{rf}$ is always parallel to A bars and symmetric to B and C bars, as shown in the inset in Fig. 3(e).

In Fig. 3(e), the FMR spectra from B and C bars indeed have a crossover at $\theta_H = 0°$ while $\mathbf{H}$ is perpendicular to A bars, as marked in the red rectangle. We further measured the fine H-θ_H spectra at different microwave frequencies, which are plotted in Figs. 3(f)–3(h). For large θ_H, the resonant modes from B and C bars are well separated, and the separation increases with $|\theta_H|$. Interestingly, the two resonant

modes merge into one single mode before $|\theta_H|$ decreases to zero. As marked by the yellow arrows in Figs. 3(f)–3(h), the angular range of the single mode strongly decreases with increasing microwave frequency f, which is $|\theta_H| < 12°$ for $f = 8$ GHz, and $|\theta_H| < 1.5°$ for $f = 10$ GHz. Such a single resonant mode within a large angular range clearly demonstrates the dynamical coupling effect between two sublattice bars. However, this coupling effect with a merging single model is different from the ordinary dynamical coupling effect, which usually causes two degenerated modes to form the avoided-crossing gap [32,33,35,45–48]. In Fig. 3(f) with $f = 8$ GHz, there is a discontinuity of the resonance at $H \sim 420$ Oe and $\theta_H \sim \pm12°$, as marked by the red arrows. Such a gap can be explained by the magnetization switching of the A bars, which changes the total effective field on B and C bars.

C. Discussion on the mode hybridization in sample No. 1

In order to better present the experimental data on the dynamical coupling effect in sample No. 1, we quantitatively analyzed the experimental spectra measured at $f = 9$ GHz by fitting the adsorption spectra with the Lorentz curves. Each adsorption peak can be fitted with the formula $\Delta S_{21} = -\sum_i \Delta I_i \frac{\Delta H_i^2}{(H - H_{r,i})^2 + \Delta H_i^2}$. Here, the index i indicates the number of the adsorption peak, H_r is resonant field, ΔH is the half-peak width, and ΔI is the amplitude of each peak. Figure 4(a) shows the typical experimental adsorption spectra at three θ_Hs and the associated fitting curves from sample No. 1. For $|\theta_H| < 3.5°$, the adsorption curves could be fitted by three Lorentz peaks, with the middle peak marked as 1, and the high- and low-field peaks marked as 2 and 3, respectively. For $|\theta_H| > 3.5°$, the adsorption curves could be fitted by two Lorentz peaks marked as 2 and 3. Figure 4(b) shows the fitted H_r as a function of θ_H. Peaks 2 and 3 are expected to be the Kittel-like bulk modes of the B and C bars, and they are well separated, indicating a strong mode hybridization with an avoided-crossing gap of ~130 Oe. Figure 4(b) also clearly demonstrates one emerging mode in the gap between peaks 2 and 3, and H_r of peak 1 slightly increases with $|\theta_H|$. Figure 4(c) shows that the fitted ΔI of peak 1 has a maximum value at $\theta_H = 0°$, and quickly decreases with $|\theta_H|$. Peaks 2 and 3 have the lowest amplitude at $\theta_H = 0°$. Note that the peak 2 with higher H_r always has larger amplitude ΔI than the peak 3 with lower H_r. We have also measured the microwave adsorption spectra by rotating a field of 1200 Oe, and the measured f-θ_H spectra also show a clear avoided-crossing gap of ~0.3 GHz and another emerging mode in the gap [49].

Next, we performed the micromagnetic simulation to understand the mode hybridization and the emerging mode in sample No. 1. The simulated field-dependent FMR spectrum of ASIs can well agree with our experimental data [49], indicating the validation of our simulation and proper choice of the simulation parameters. We gradually changed θ_H to investigate the dynamical coupling effect among the degenerated modes located in different sublattice bars. The variation of the field orientation is expected to break the degeneracy of the dynamical states in different bars. As shown in Fig. 4(d), the applied field gradually varies from -3000 to $+3000$ Oe with a fixed θ_H, and an in-plane field pulse $h(t)$ is
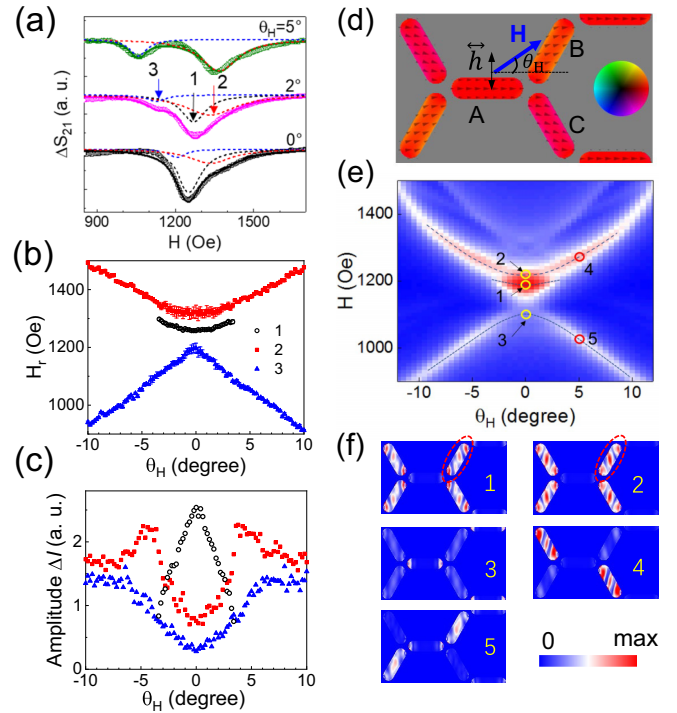
FIG. 4. (a) Typical adsorption spectra and the fitting curves at different θ_Hs for sample No. 1 at $f = 9$ GHz. (b), (c) Fitted θ_H-dependent (b) resonant field H_r and (c) peak intensity ΔI of three peaks in the FMR spectra for sample No. 1. (d) Simulated magnetization distribution in kagome ASI at $\theta_H = 0°$ after the field was swept from -3000 to $+1200$ Oe; the different colors indicate the in-plane orientations of magnetization in kagome ASI bars as the color wheel plotted. (e) Surface plots of the simulated H-θ_H FMR spectra with $f = 9$ GHz; simulation geometry is shown in (d). The applied field rotates around the directions of H/A bars with different θ_H. (f) Representative spatial distributions of magnetization dynamics at positions 1–5 marked in (e). Red dashed ellipses emphasize the different magnetization distributions at positions 1 and 2.

applied to simulate the time-dependent magnetization $m_z(t)$; then, the frequency-dependent power spectrum density (PSD) spectrum can be obtained through the Fourier transformation. Figure 4(e) displays the simulated amplitude at $f = 9$ GHz in the PSD spectrum as a function of H and θ_H. As indicated by the dashed lines, there are three major magnon modes for $H \sim 1200$ Oe. The upper branch with higher H_r and the lower branch with lower H_r show the clear avoided-crossing behavior, and the middle branch with the strongest dynamical amplitude only exists for $|\theta_H| < 3°$, which well reproduces the experimental results in Fig. 3(c). Several weak spin-wave modes for $H > 1250$ Oe are too weak to be observed experimentally. For $|\theta_H| > 3°$, the upper-branch mode always has stronger dynamical amplitude than the lower-branch mode.

We also simulated the lateral dynamical magnetization distribution at different resonant conditions as marked by the open circles in Fig. 4(e). For the positions 1–3 with $\theta_H = 0°$, the resonant dynamical magnetization locates symmetrically in both B and C bars. For the position 4 in higher H_r mode and the position 5 in lower H_r mode at $\theta_H = 5°$, the field breaks the degeneracy of the magnon modes in B and C bars;

thus, the simulated dynamical magnetization locates mainly in either B or C bars. As discussed in Ref. [33], the measured bulk mode could be the combination of standing spin wave and edge mode, so all the dynamical magnetization distributions in Fig. 4(f) clearly show several nodes. However, as indicated by the dashed ellipses in Fig. 4(f) the dynamical magnetization distribution at position 1 contains four nodes in one bar, but all the dynamical magnetization distributions at positions 2–5 contain three nodes. So, the magnon mode at $\theta_H \sim 0°$ of the middle branch is different from the upper- and lower-branch magnon modes, and the emerging of this mode may suppress the other two modes, in good agreement with the experimental results in Fig. 4(c) that both upper and lower modes have the reduced dynamical magnetization amplitude at $\theta_H \sim 0°$. Our results also indicate that all three magnon modes are actually coupled together through the stray field. Note that both experimental results in Figs. 3(b)–3(d) and the simulation results show that the emerging middle-branch mode always exists independent of the field strength; thus, it is difficult to identify the existence of this magnon mode by the ordinary field-dependent dynamical measurement without carefully varying the field orientation.

D. Discussion of the observed merging mode in sample No. 2

Next, we will discuss the origin of the observed merging mode in sample No. 2 shown in Figs. 3(e)–3(h). We first perform the quantitative analysis of the FMR spectra measured from sample No. 2 at $f = 9$ GHz, as shown in Figs. 5(a)–5(c). Figure 5(a) shows the typical experimental adsorption spectra and the associated fitting curves. For $|\theta_H| < 2.5°$, one single peak (marked as 1) can well fit the experimental curves, and for $|\theta_H| > 2.5°$, it requires two separated peaks marked as 2 and 3 to obtain the reasonable fitting. In Fig. 5(b), the fitted H_r of two resonant modes gradually merge into one mode with a single H_r, which slightly decreases with $|\theta_H|$. Figure 5(c) shows that the fitted amplitude of peak 1 for $|\theta_H| < 2.5°$ is comparable with the sum of the amplitudes of peaks 2 and 3. For $|\theta_H| > 2.5°$, the amplitude of peak 3 with lower H_r is always larger than that of peak 2 with higher H_r. The fitted half-peak width ΔH is larger than 40 Oe for all the resonant modes.

In order to understand the experimental results with a merging single mode at $\theta_H \sim 0°$ from sample No. 2, we also simulated the dynamical properties for **H** varying nearly perpendicular to one of the sublattice bars as shown in Fig. 4(d). Figure 4(e) shows the simulated PSD amplitude with $f = 9$ GHz as functions of H and θ_H, and the two dynamical modes clearly merge into one single mode at $H \sim 600$ Oe for $|\theta_H| < 3°$, which well agrees with the experimental data in Fig. 5(b). For $|\theta_H| > 3°$, the upper-branch mode with higher H_r has lower intensity than the lower-branch mode, which is also consistent with the fitting results in Fig. 5(c). The red arrows in Fig. 5(e) mark the discontinuity at $H \sim 700$ Oe and $|\theta_H| \sim 10°$ in the high-energy mode, which is attributed to the magnetization reversal of A bars. The reversal field of A bars should be larger for smaller $|\theta_H|$. So, our simulations prove that the magnetic state in A bars also influences the dynamical properties in B and C bars.
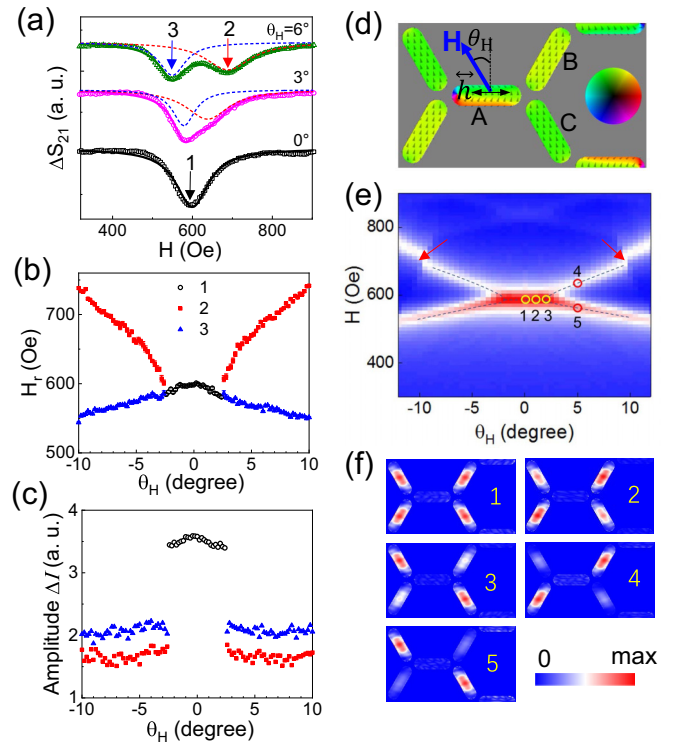
FIG. 5. (a) Typical adsorption spectra and the fitting curves at different θ_H for sample No. 2 at $f = 9$ GHz. (b), (c) Fitted θ_H-dependent (b) resonant field H_r and (c) peak intensity ΔI of three peaks in the FMR spectra for sample No. 2. (d) Simulated magnetization distribution in kagome ASI at $\theta_H = 0°$ after the field was swept from -3000 to $+600$ Oe; the different colors indicate the in-plane orientations of magnetization in kagome ASI bars as the color wheel plotted. (e) Surface plots of the simulated H-θ_H FMR spectra with $f = 9$ GHz. Red arrows indicate the discontinuity induced by the magnetization switching in the A bars. Simulation geometry is shown in (d), and the applied field rotated around the directions of $H \perp A$ bars with different θ_H. (f) Representative spatial distributions of magnetization dynamics at positions 1–5 marked in (e).

Figure 5(f) shows the simulated lateral dynamical magnetization distributions at different resonant conditions in the f-θ_H spectra in Fig. 4(e). At positions 1–3 for $|\theta_H| < 3°$, the dynamical magnetization locates inside both B and C bars, but for positions 4 and 5 with $\theta_H = 5°$, the dynamical magnetization mainly locates in either B or C bars. All the dynamical magnetizations locate in the center of each magnetic bar with a single node.

The dynamical coupling between two degenerate magnon modes usually induces an avoided-crossing gap between two magnon modes [35,45–48]; thus, it is nontrivial that two magnon modes merge into one single mode shown in Figs. 3 and 5. So, the merging mode measured in sample No. 2 may be induced not by the dynamical coupling, but by the static dipolar coupling effect between different magnetic bars. It is well known that the magnetization dynamical procession is determined by $\frac{d\vec{M}}{dt} = \gamma \vec{M} \times \vec{H}_{\text{eff}}$, with γ as the Gilbert gyromagnetic ratio and H_{eff} as the static effective field including the external field and the stray fields. The static stray field from the different magnetic bars may generate the same H_{eff}
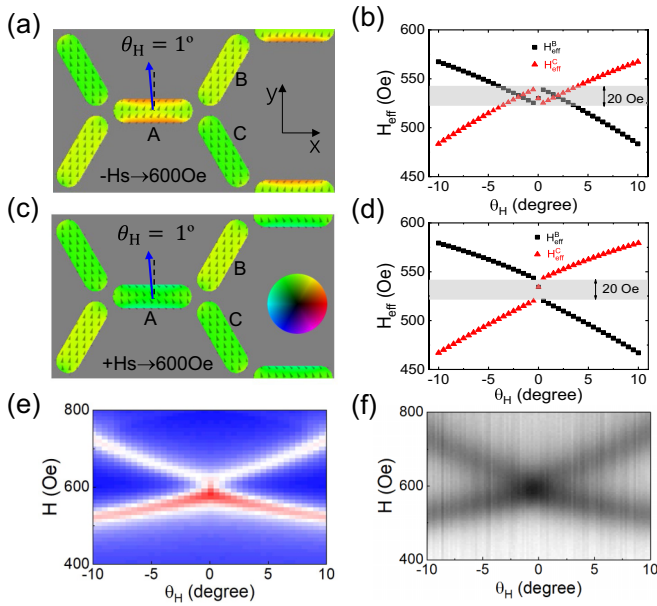
FIG. 6. (a), (c) Simulated magnetization distributions in kagome ASI at $H = 600$ Oe after the field was swept (a) from -3000 to $+600$ Oe and (c) from $+3000$ to $+600$ Oe, respectively. The blue arrow shows the field direction at $\theta_H = 1°$. (b), (d) Total effective fields H_{eff}^B and H_{eff}^C at the center of B and C bars with $H = 600$ Oe as a function of θ_H. The field was swept (b) from -3000 to $+600$ Oe and (d) from $+3000$ to $+600$ Oe, respectively. (e) Simulated and (f) experimental H-θ_H spectra with different θ_H at $f = 9$ GHz, and the applied field was swept from $+3000$ Oe.

in B and C bars with little evolution with the field orientation; then, the single resonant peak at $\theta_H \sim 0°$ can be explained. The H_{eff} in B and C bars can be calculated through the micromagnetic simulation. In the simulation, for each θ_H, we first sweep the field from -3000 to $+600$ Oe, and then quantify the H_{eff} in B and C bars. Figure 6(a) shows the typical micromagnetic state at $H = +600$ Oe with $\theta_H = 1°$, which shows that the magnetization in an A bar has a certain $+x$ component. Such magnetization with a $+x$ component can provide the opposite effect on the effective field H_{eff} in B and C bars. Figure 6(b) shows the calculated θ_H-dependent H_{eff} in the center of B and C bars, and indeed for $|\theta_H| < 3°$, the difference between the effective fields in B and C bars have is less than 20 Oe. Such difference of H_{eff} is smaller than the width of the resonant peak; thus, only one merging single peak can be observed for $|\theta_H| < 3°$, consistent with our experimental and simulation results [49].

We further studied the effect of the stray field from A bars by sweeping the field from $+3000$ to $+600$ Oe with $\theta_H = 1°$. Figure 6(c) shows that the magnetization in the A bars has the $-x$ component, different from that in Fig. 6(a), but the magnetization distributions in B and C bars are almost the same as in Fig. 6(a). The opposite x-component magnetization in A bars provides the opposite stray field in B and C bars; thus, the calculated H_{eff} in B and C bars in Fig. 6(d) always

has the difference larger than 20 Oe for $\theta_H \neq 0°$. Accordingly, the simulated PSD amplitude as a function of H and θ_H in Fig. 6(e) does not contain the merging single peak, and the two resonant peaks are well separated except at $\theta_H = 0°$. We also performed the experiment on sample No. 2 with the field swept from $+3000$ Oe, and only a single crossing of the resonant modes from B and C bars can be observed in Fig. 6(f). So, our studies demonstrate that the micromagnetic states in ASIs indeed influence the dynamical properties of ASIs, which is important for the reconfigurable magnonic crystals in information-processing applications.

On the other hand, although the observed merging single mode in sample No. 2 is induced by the static stray field, the effect of the dynamical coupling on the magnon modes in B and C bars still exists. As shown in Figs. 5(e) and 6(e), the upper branch always has a lower magnon amplitude than the lower branch, indicating that the dynamical coupling makes the bulk modes in B and C bars to be out-of-phase coupled in the upper branch, and to be in-phase coupled in the lower branch [33].

IV. CONCLUSION

In summary, we have comprehensively studied magnetic dynamics in a disconnect kagome ASI lattice using the broadband FMR method and micromagnetic simulation. By gradually varying the orientation of the applied magnetic field in the sample plane, we continuously tuned the resonance modes of the nanomagnets, and observed two types of magnon coupling effect due to the dipolar interaction between the magnetizations in different sublattice bars. For the field parallel to one sublattice bar, the dynamical modes from the other two sublattice bars show a strong coupling effect, which not only induces the mode hybridization with an avoided-crossing gap, but also induces an emerging dynamical magnon mode. For the field perpendicular to one sublattice bar, the dynamics modes from the other two sublattice bars can merge into a single mode due to the static stray field among the sublattice bars. Our studies confirm that the coupling effect strongly depends on the micromagnetic states, thus also depends on the history of the magnetizing process. Our results reveal that both static and dynamical dipolar interactions can affect the coupling among different magnon modes, which is important for designing reprogrammable magnonics devices based on two-dimensional periodic arrays.

[1] L. J. Heyderman and R. L. Stamps, Artificial ferroic systems: Novel functionality from structure, interactions and dynamics, J. Phys.: Condens. Matter **25**, 363201 (2013).

[2] C. Nisoli, R. Moessner, and P. Schiffer, Colloquium: Artificial spin ice: Designing and imaging magnetic frustration, Rev. Mod. Phys. **85**, 1473 (2013).

[3] R. F. Wang, C. Nisoli, R. S. Freitas, J. Li, W. McConville, B. J. Cooley, M. S. Lund, N. Samarth, C. Leighton, V. H. Crespi, and P. Schiffer, Artificial "spin ice" in a geometrically frustrated lattice of nanoscale ferromagnetic islands, Nature (London) **439**, 303 (2006).

[4] G. Moller and R. Moessner, Artificial Square Ice and Related Dipolar Nanoarrays, Phys. Rev. Lett. **96**, 237202 (2006).

[5] C. Castelnovo, R. Moessner, and S. L. Sondhi, Magnetic monopoles in spin ice, Nature (London) **451**, 42 (2008).

[6] E. Mengotti, L. J. Heyderman, A. Fraile Rodriguez, A. Bisig, L. Le Guyader, F. Nolting, and H. B. Braun, Building blocks of an artificial kagome spin ice: Photoemission electron microscopy of arrays of ferromagnetic islands, Phys. Rev. B **78**, 144402 (2008).

[7] E. Mengotti, L. J. Heyderman, A. F. Rodriguez, F. Nolting, R. V. Huegli, and H.-B. Braun, Real-space observation of emergent magnetic monopoles and associated Dirac strings in artificial kagome spin ice, Nat. Phys. **7**, 68 (2011).

[8] J. P. Morgan, A. Stein, S. Langridge, and C. H. Marrows, Thermal ground-state ordering and elementary excitations in artificial magnetic square ice, Nat. Phys. **7**, 75 (2011).

[9] S. A. Daunheimer, O. Petrova, O. Tchernyshyov, and J. Cumings, Reducing Disorder in Artificial Kagome Ice, Phys. Rev. Lett. **107**, 167201 (2011).

[10] Y. Qi, T. Brintlinger, and J. Cumings, Direct observation of the ice rule in an artificial kagome spin ice, Phys. Rev. B **77**, 094418 (2008).

[11] U. B. Arnalds, A. Farhan, R. V. Chopdekar, V. Kapaklis, A. Balan, E. T. Papaioannou, M. Ahlberg, F. Nolting, L. J. Heyderman, and B. Hjorvarsson, Thermalized ground state of artificial kagome spin ice building blocks, Appl. Phys. Lett. **101**, 112404 (2012).

[12] K. Zeissler, S. K. Walton, S. Ladak, D. E. Read, T. Tyliszczak, L. F. Cohen, and W. R. Branford, The non-random walk of chiral magnetic charge carriers in artificial spin ice, Sci. Rep. **3**, 1252 (2013).

[13] J. Sklenar, V. S. Bhat, L. E. DeLong, and J. B. Ketterson, Broadband ferromagnetic resonance studies on an artificial square spin-ice island array, J. Appl. Phys. **113**, 17b530 (2013).

[14] E. Iacocca, S. Gliga, R. L. Stamps, and O. Heinonen, Reconfigurable wave band structure of an artificial square ice, Phys. Rev. B **93**, 134420 (2016).

[15] M. B. Jungfleisch, W. Zhang, E. Iacocca, J. Sklenar, J. Ding, W. Jiang, S. Zhang, J. E. Pearson, V. Novosad, J. B. Ketterson, O. Heinonen, and A. Hoffmann, Dynamic response of an artificial square spin ice, Phys. Rev. B **93**, 100401(R) (2016).

[16] S. H. Skjaervo, C. H. Marrows, R. L. Stamps, and L. J. Heyderman, Advances in artificial spin ice, Nat. Rev. Phys. **2**, 13 (2020).

[17] S. Lendinez and M. B. Jungfleisch, Magnetization dynamics in artificial spin ice, J. Phys.: Condens. Matter **32**, 013001 (2020).

[18] G. Carlotti, G. Gubbiotti, M. Madami, S. Tacchi, F. Hartmann, M. Emmerling, M. Kamp, and L. Worschech, From micro- to nanomagnetic dots: Evolution of the eigenmode spectrum on

reducing the lateral size, J. Phys. D: Appl. Phys. **47**, 265001 (2014).

[19] V. S. Bhat, F. Heimbach, I. Stasinopoulos, and D. Grundler, Angular-dependent magnetization dynamics of kagome artificial spin ice incorporating topological defects, Phys. Rev. B **96**, 014426 (2017).

[20] B. Rana, A. K. Mondal, S. Bandyopadhyay, and A. Barman, Applications of nanomagnets as dynamical systems: I, Nanotechnology **33**, 062007 (2022).

[21] B. Rana, A. K. Mondal, S. Bandyopadhyay, and A. Barman, Applications of nanomagnets as dynamical systems: II, Nanotechnology **33**, 082002 (2022).

[22] S. Gliga, E. Iacocca, and O. G. Heinonen, Dynamics of reconfigurable artificial spin ice: Toward magnonic functional materials, APL Mater. **8**, 040911 (2020).

[23] W. Bang, F. Montoncello, M. B. Jungfleisch, A. Hoffmann, L. Giovannini, and J. B. Ketterson, Angular-dependent spin dynamics of a triad of permalloy macrospins, Phys. Rev. B **99**, 014415 (2019).

[24] X. Zhou, G.-L. Chua, N. Singh, and A. O. Adeyeye, Large area artificial spin ice and anti-spin ice Ni80Fe20 Structures: Static and dynamic behavior, Adv. Funct. Mater. **26**, 1437 (2016).

[25] Y. Li, G. Gubbiotti, F. Casoli, F. J. T. Goncalves, S. A. Morley, M. C. Rosamond, E. H. Linfield, C. H. Marrows, S. McVitie, and R. L. Stamps, Brillouin light scattering study of magnetic-element normal modes in a square artificial spin ice geometry, J. Phys. D: Appl. Phys. **50**, 015003 (2017).

[26] J. Dubowik, P. Kuswik, M. Matczak, W. Bednarski, F. Stobiecki, P. Aleshkevych, H. Szymczak, M. Kisielewski, and J. Kisielewski, Ferromagnetic resonance and resonance modes in kagome lattices: From an open to a closed kagome structure, Phys. Rev. B **93**, 224423 (2016).

[27] V. S. Bhat and D. Grundler, Tuning interactions in reconfigurable kagome artificial spin ices for magnonics, Appl. Phys. Lett. **119**, 092403 (2021).

[28] T. Dion, D. M. Arroo, K. Yamanoi, T. Kimura, J. C. Gartside, L. F. Cohen, H. Kurebayashi, and W. R. Branford, Tunable magnetization dynamics in artificial spin ice via shape anisotropy modification, Phys. Rev. B **100**, 054433 (2019).

[29] F. Montoncello, L. Giovannini, W. Bang, J. B. Ketterson, M. B. Jungfleisch, A. Hoffmann, B. W. Farmer, and L. E. De Long, Mutual influence between macrospin reversal order and spin-wave dynamics in isolated artificial spin-ice vertices, Phys. Rev. B **97**, 014421 (2018).

[30] V. S. Bhat, S. Watanabe, K. Baumgaertl, A. Kleibert, M. A. W. Schoen, C. A. F. Vaz, and D. Grundler, Magnon Modes of Microstates and Microwave-Induced Avalanche in Kagome Artificial Spin Ice with Topological Defects, Phys. Rev. Lett. **125**, 117208 (2020).

[31] W. Bang, J. Sturm, R. Silvani, M. T. Kaffash, A. Hoffmann, J. B. Ketterson, F. Montoncello, and M. B. Jungfleisch, Influence of the Vertex Region on Spin Dynamics in Artificial Kagome Spin Ice, Phys. Rev. Appl. **14**, 014079 (2020).

[32] J. C. Gartside, A. Vanstone, T. Dion, K. D. Stenning, D. M. Arroo, H. Kurebayashi, and W. R. Branford, Reconfigurable magnonic mode-hybridisation and spectral control in a bicomponent artificial spin ice, Nat. Commun. **12**, 2488 (2021).

[33] T. Dion, J. C. Gartside, A. Vanstone, K. D. Stenning, D. M. Arroo, H. Kurebayashi, and W. R. Branford, Observation and

control of collective spin-wave mode hybridization in chevron arrays and in square, staircase, and brickwork artificial spin ices, Phys. Rev. Res. **4**, 013107 (2022).

[34] B. Pigeau, C. Hahn, G. de Loubens, V. V. Naletov, O. Klein, K. Mitsuzuka, D. Lacour, M. Hehn, S. Andrieu, and F. Montaigne, Measurement of the Dynamical Dipolar Coupling in a Pair of Magnetic Nanodisks Using a Ferromagnetic Resonance Force Microscope, Phys. Rev. Lett. **109**, 247602 (2012).

[35] P.-C. Xu, J. W. Rao, Y. S. Gui, X. Jin, and C. M. Hu, Cavity-mediated dissipative coupling of distant magnetic moments: Theory and experiment, Phys. Rev. B **100**, 094415 (2019).

[36] D. M. Burn, M. Chadha, and W. R. Branford, Angular-dependent magnetization reversal processes in artificial spin ice, Phys. Rev. B **92**, 214425 (2015).

[37] D. Shi, H. Chen, J. Xu, H. Xia, Y. Chen, and Y. Wu, Kerr microscopy real-time imaging of the magnetization reversal process in kagome artificial spin ice, Phys. Rev. B **101**, 134428 (2020).

[38] W. Bang, F. Montoncello, M. T. Kaffash, A. Hoffmann, J. B. Ketterson, and M. B. Jungfleisch, Ferromagnetic resonance spectra of permalloy nano-ellipses as building blocks for complex magnonic lattices, J. Appl. Phys. **126**, 203902 (2019).

[39] L. Sun, C. Zhou, J. H. Liang, T. Xing, N. Lei, P. Murray, K. Liu, C. Won, and Y. Z. Wu, Magnetization reversal in kagome artificial spin ice studied by first-order reversal curves, Phys. Rev. B **96**, 144409 (2017).

[40] A. Vansteenkiste, J. Leliaert, M. Dvornik, M. Helsen, F. Garcia-Sanchez, and B. Van Waeyenberge, The design and verification of MuMax3, AIP Adv. **4**, 107133 (2014).

[41] J. Mulkers, B. van Waeyenberge, and M. V. Milosevic, Effects of spatially engineered Dzyaloshinskii-Moriya interaction in ferromagnetic films, Phys. Rev. B **95**, 144401 (2017).

[42] J.-V. Kim, F. Garcia-Sanchez, J. Sampaio, C. Moreau-Luchaire, V. Cros, and A. Fert, Breathing modes of confined skyrmions in ultrathin magnetic dots, Phys. Rev. B **90**, 064410 (2014).

[43] J. Ding, M. Kostylev, and A. O. Adeyeye, Broadband ferromagnetic resonance spectroscopy of permalloy triangular nanorings, Appl. Phys. Lett. **100**, 062401 (2012).

[44] T. Seki, K. Utsumiya, Y. Nozaki, H. Imamura, and K. Takanashi, Spin wave-assisted reduction in switching field of highly coercive iron-platinum magnets, Nat. Commun. **4**, 1726 (2013).

[45] S. Klingler, V. Amin, S. Gepraegs, K. Ganzhorn, H. Maier-Flaig, M. Althammer, H. Huebl, R. Gross, R. D. McMichael, M. D. Stiles, S. T. B. Goennenwein, and M. Weiler, Spin-Torque Excitation of Perpendicular Standing Spin Waves in Coupled YIG/Co heterostructures, Phys. Rev. Lett. **120**, 127201 (2018).

[46] J. Chen, C. Liu, T. Liu, Y. Xiao, K. Xia, G. E. W. Bauer, M. Wu, and H. Yu, Strong Interlayer Magnon-Magnon Coupling in Magnetic Metal-Insulator Hybrid Nanostructures, Phys. Rev. Lett. **120**, 217202 (2018).

[47] D. MacNeill, J. T. Hou, D. R. Klein, P. Thang, P. Jarillo-Herrero, and L. Liu, Gigahertz Frequency Antiferromagnetic Resonance and Strong Magnon-Magnon Coupling in the Layered Crystal CrCl3, Phys. Rev. Lett. **123**, 047204 (2019).

[48] M. Harder and C.-M. Hu, Cavity spintronics: An early review of recent progress in the study of magnonphoton level repulsion, in *Solid State Physics*, edited by R. E. Camley and R. L. Stamps, Vol 69 (Academic Press, 2018), pp. 47–121.

[49] See Supplemental Material at http://link.aps.org/supplemental/10.1103/PhysRevB.106.144413 for the simulation of the field-dependent FMR spectrum, the f-θ_H spectra measured by rotating a fixed field, and calculation of static magnetic dipole field in kagome ASIs in sample No. 1.